ELSEVIER

Journal of Power Sources 102 (2001) 144–154

JOURNAL OF POWER SOURCES

www.elsevier.com/locate/jpowsour

3-D model calculation for planar SOFC

H. Yakabe*, T. Ogiwara, M. Hishinuma, I. Yasuda

Fundamental Technology Research Laboratory, Tokyo Gas Co., Ltd., 16-25, Shibaura, 1-chome, Minato-ku, Tokyo 105-0023, Japan

Received 22 August 2000; received in revised form 20 December 2000; accepted 5 April 2001

Abstract

A three-dimensional mathematical model for a planar SOFC was constructed. The concentrations of the chemical species, the temperature distribution, the potential distribution, and the current density were calculated using a single-unit model with double channels of co-flow or counter-flow pattern. The finite volume method was employed for the calculation, which is based on the fundamental conservation laws of mass, energy, and electrical charge. The internal or external steam-reforming, the water-shift reaction, and the diffusion of gases in the porous electrodes were taken into the model. The effects of the cell size, the operating voltage and the thermal conductivity of the cell components on the calculated results were investigated. From the simulated temperature distributions in the electrolyte and the interconnector, the stress distributions were calculated using the finite element method. The results demonstrated that the steam reforming would generate internal stresses of several tens MPa in an electrolyte.

Keywords: Planar SOFC; 3-D model; Thermal conductivity; Thermal stress; Cell performance

1. Introduction

The solid oxide fuel cells (SOFCs) are promising candidates for future energy conversion systems because of their higher energy conversion efficiency than those for conventional heat engine systems and other types of fuel cells. In addition, internal reforming of natural gas can be performed at the anode, which allows direct use of natural gas as the fuel.

In SOFC stack designs, the planar type design has received much attention recently, because it is simpler to fabricate and easier to be made into various shapes than the other type designs. Besides, the planar type SOFC offers higher power density relative to the tubular type SOFC, which is ascribed to the low electrical resistance due to shorter current paths. However, the status of the development is still at a module level, and some technical issues have not been solved yet. The internal stresses in cell components arising from thermal shocks or heat cycles are one of the problems to be solved. The planar type SOFC requires high temperature gas seals at the edges or around the internal gas manifolds. For this purpose, cement, glass and glass-ceramic seals are expected to give sufficient sealing efficiency. However, the strict binding among each cell component generates mechanical constraints, and thus a slight mismatch in thermal expansion coefficient (TEC) among the cell components can cause a large stress. Moreover, because of non-homogeneous temperature distributions inside the cell, cell components are irregularly deformed, adding a large internal stress. As a consequence, the thermal expansion coefficient matching among the cell components and mitigation of the non-homogeneous temperature distributions in the cell components are indispensable to reduce the internal stress. Some parameters of stack design and operating conditions, such as cell geometry, internal or external steam reforming, thermal conductivity of the components, and cell operating voltage affect the temperature distributions inside the cells in a complicated way, and thus it is difficult to optimize these parameters independently to lower the internal stresses. The computer simulation technique has been used to investigate the cell performance in SOFCs, and considered to be an effective way to analyze the effects of these parameters on the temperature distributions inside the cells [1–8]. However, only a few analyses on the internal stresses have been developed from the cell performance analyses [9,10] because fully three-dimensional (3-D) model is required for the 3-D stress calculation.

The purpose of the present work is to estimate the thermal stresses in the cell components using a 3-D model simulation. In order to derive the stresses, we calculated the temperature distributions in the cell components in the first step. We employed simplified single-unit models with

* Corresponding author. Fax: +81-3-3453-7583.
E-mail address: yakabe@tokyo-gas.co.jp (H. Yakabe).

0378-7753/01/$ – see front matter
PII: S0378-7753(01)00792-3

Nomenclature

F_{hj}	diffusional energy flux in direction x_j
$\sqrt{g}$	determinant of metric tensor
h	$h_t + \sum m_m H_m$
h_t	thermal enthalpy
H_A	total enthalpy of air in the channel
H_F	total enthalpy of fuel in the channel
H_m	heat of formation of constituent m
H_S	enthalpy in the electrolyte
m_m	mass fraction of mixture constituent m
M_A	total mass of air in the channel
M_F	total mass of fuel in the channel
n	unit vector normal to the boundary
p	piezometric pressure
q	heat loss term
Q	heat source term
s_h	energy source
s_i	momentum source components
S_i	rate of production or consumption of species i
t	time
T	temperature
u_i	absolute fluid velocity component in direction x_i
$\tilde{u}_j$	relative velocity between fluid and local co-ordinate frame that moves with velocity u_{cj}
x_i	Cartesian coordinate ($i = 1, 2, 3$)

Greek letters

λ	thermal conductivity
κ	heat transfer coefficient
ρ	density
τ_{ij}	stress tensor component

co-flow or counter-flow bipolar channels, and calculated the concentrations of the chemical species, the potential distribution, the local and average current density, and the temperature distribution inside the cell. The simulation model was constructed in detail to include the internal or external steam-reforming, the water-shift reaction, and the diffusion of the gaseous species in the porous electrodes. In the second step the tensile stresses in the cell components were computed from the temperature profiles. The internal stresses were estimated as a function of the cell size, the operating voltage, and the thermal conductivity of the cell components, and thus suitable operating conditions to reduce the internal stresses were proposed.

2. Mathematical model

2.1. Model geometry

In general, one cell-stack is constructed from a cell (anode/electrolyte/cathode) and an inter-connector. As guides of an air and a fuel to the cell, an inter-connector with channel ribs is employed. The cell-stack is assembled using separators as an auxiliary, and air and fuel manifolds are formed to introduce the air and the fuel. Fig. 1 shows the schematic diagram of a cell-stack with internal manifolds formed in the separators. Since a lot of time is needed to simulate the cell performance for the whole stack, a simplified single-unit cell model with bipolar channels was used in the present simulation. Only the counter-flow and the co-flow model were considered because numerous meshes are necessary to model the cross-flow pattern and thus the calculating time becomes enormous. Further, for the sake of simplicity in the calculation, we analyzed half of the one repeating unit located in the middle part of one center stack. The one cell-stack and the single-unit model are illustrated in Fig. 2. In this model, the thickness of the electrolyte, cathode, and anode are 0.1, 0.15, and 0.1 mm, respectively.

2.2. Thermo-fluid model

The thermo-fluids analysis was performed using the computational fluid dynamics tool 'STAR-CD' (Computational Dynamics Ltd.). In STAR-CD, the algebraic finite-volume equations are solved. The solid and fluid parts were divided into small discrete meshes, and in each mesh, the following differential equations governing the conservation of mass, momentum, and energy were solved.

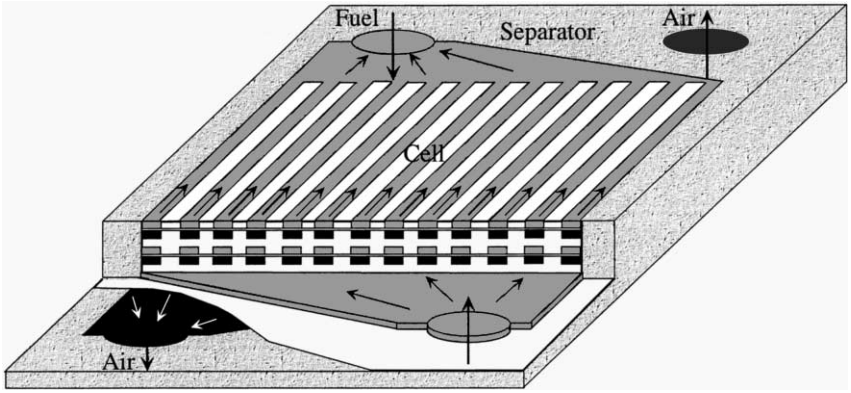

Fig. 1. The schematic diagram of the cell-stack with internal manifolds.

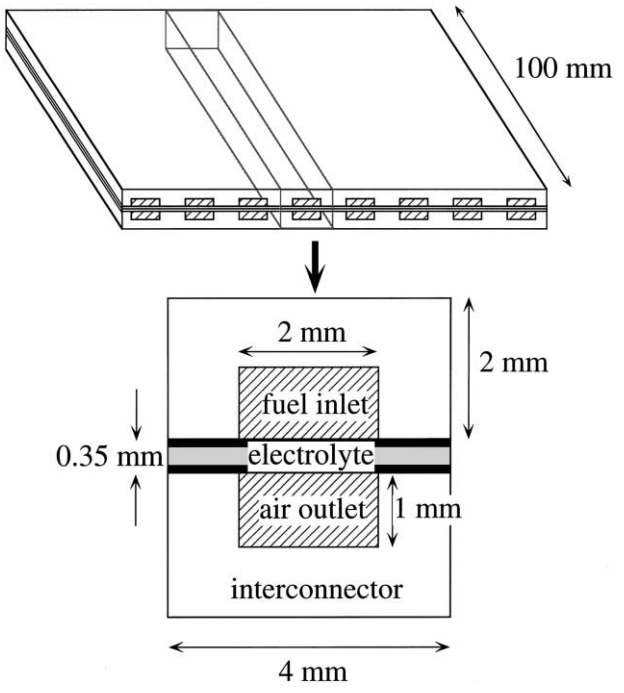

Fig. 2. The illustrations of the one cell-stack and the single-unit model used for the simulation.

- The mass and momentum conservation (the 'Navier–Stokes' equations):

$$\frac{1}{\sqrt{g}}\frac{\partial}{\partial t}(\sqrt{g}\rho u_j)+\frac{\partial}{\partial x_j}(\rho\tilde{u}_j u_i-\tau_{ij})=-\frac{\partial p}{\partial \mathrm{x}_i}+s_i \tag{1}$$

- The enthalpy conservation equation:

$$\frac{1}{\sqrt{g}}\frac{\partial}{\partial t}(\sqrt{g}\rho h)+\frac{\partial}{\partial x_j}(\rho\tilde{u}_j h-F_{hj}) =\frac{1}{\sqrt{g}}\frac{\partial}{\partial t}(\sqrt{g}p)+u_j\frac{\partial p}{\partial x_j}+\tau_{ij}\frac{\partial u_i}{\partial x_j}+s_h \tag{2}$$

The specific heat of the fluid was treated as the polynomial function of the temperature, while the thermal conductivity of the fluid and the solid, and the specific heat of the solid part were assumed to be independent of the temperature.

For the whole model, the following mass and energy balances should be considered.

- The mass balance of the total gas:

$$\frac{\mathrm{d}M_\mathrm{A}}{\mathrm{d}t}=M_\mathrm{A}^\mathrm{IN}-M_\mathrm{A}^\mathrm{OUT}+\sum_i S_i^\mathrm{A}$$
$$\frac{\mathrm{d}M_\mathrm{F}}{\mathrm{d}t}=M_\mathrm{F}^\mathrm{IN}-M_\mathrm{F}^\mathrm{OUT}+\sum_\mathrm{i} S_i^\mathrm{F} \tag{3}$$

- The enthalpy balance:

$$\frac{\mathrm{d}H_\mathrm{F}}{\mathrm{d}t}=H_\mathrm{F}^\mathrm{IN}-H_\mathrm{F}^\mathrm{OUT}+Q_\mathrm{F}-q_\mathrm{F}-q_\mathrm{F}^\mathrm{EXT}$$
$$\frac{\mathrm{d}H_\mathrm{A}}{\mathrm{d}t}=H_\mathrm{A}^\mathrm{IN}-H_\mathrm{A}^\mathrm{OUT}+Q_\mathrm{A}-q_\mathrm{A}-q_\mathrm{A}^\mathrm{EXT} \tag{4}$$
$$\frac{\mathrm{d}H_S}{\mathrm{d}t}=Q_S+q_\mathrm{A}+q_\mathrm{F}-q_S^\mathrm{EXT}$$

As mentioned above, in this simulation we selected and modeled one repeating unit located in the middle part of the center stack. At the middle part of the center stack, the boundaries between the single-unit and the adjacent units are regarded to be thermally adiabatic. Hence, for the thermal boundary conditions at the surfaces of the solid part connecting to the next units, adiabatic boundary conditions were employed. In a practical cell stack, the fuel and the air are introduced into the channel through manifolds. For the cell-stack illustrated in Fig. 1, there are horizontal guide parts formed by the separators from the manifolds to the channels. The edge parts of the single-unit faces to the guide parts and the heat exchange between the edge parts and the environment around the stack is indirect. As it is difficult to determine the exact boundary condition at the edge parts, we employed the adiabatic boundary condition at the edge parts. For the boundary between the solid and the fluid, the following continuity condition was imposed:

$$[\lambda(x)\nabla T_\mathrm{s}(x)]\times n=\kappa[T_\mathrm{f}(x)-T_\mathrm{s}(x)] \tag{5}$$

where n is the unit vector normal to the boundary, T_s and T_f being temperature of the solid and fluid at x on the boundary, respectively.

Cell-stacks are usually operated at 900–1000°C, and at such high temperatures a radiant heat exchange would have an essential effect on the heat exchange inside the channels. Hence, in this study, we investigated the effect of the radiant heat exchange inside the channels on the simulated results. To calculate the radiant heat exchange inside the channels, the boundaries of the calculation domain were all subdivided into contiguous non-overlapping areas 'patches'. From the nominal center of each patch a number of beams were emitted and the each beam was traced through the fluid until it intercepted an opposing patch. Assumed grey body surfaces, for small areas $\mathrm{d}A_i$ and $\mathrm{d}A_j$ shown in Fig. 3, the amount of radiant energy transfer to or from each patch was then calculated from the radiant transport equation:

$$\mathrm{d}q_{i-j}=\cos\phi_i\cos\phi_j\frac{\mathrm{d}A_i\mathrm{d}A_j}{\pi r^2}\varepsilon_i\varepsilon_j(E_i-E_j) \tag{6}$$

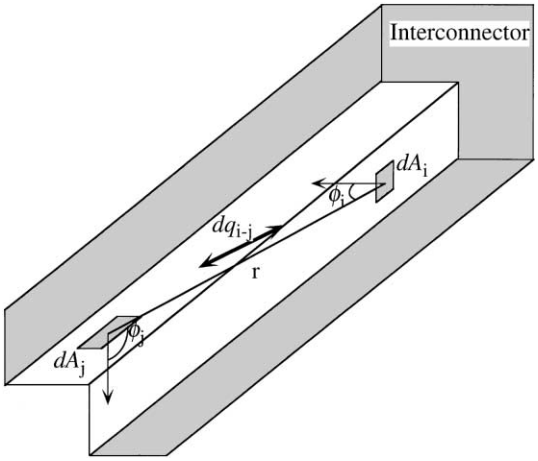

Fig. 3. The illustration of the radiant heat exchange inside the channel.

where dq_{i-j} is the net energy exchange between patch i and patch j, r is the distance between the patches, E_i and E_j are the radiation energy of patches i and j, respectively, ϕ_i and ϕ_j are the angles between a normal to the surface and the line drawn between the patches, and ε_i and ε_j are the surface emissivity for the patches i and j. Using the Stefan–Boltzmann law

$$E = \sigma T^4 \tag{7}$$

where σ is the Stefan–Boltzmann constant, Eq. (6) is rewritten as

$$dq_{i-j} = \cos\phi_i \cos\phi_j \frac{dA_i dA_j}{\pi r^2} \varepsilon_i \varepsilon_j \sigma (T_i^4 - T_j^4) \tag{8}$$

where T_i and T_j are the surface temperatures at the patches i and j, respectively. For all the patches the net energy exchange written by Eq. (8) should be calculated. In the present model, the effect of the radiant heat exchange on the heat balance inside the channels is considered to be small. Because the channel length along the fluid flow is extremely long compared with the size of the channel cross section. When dealing with the radiant heat exchange patches, the temperatures vary between high and low. ϕ_i and ϕ_j in Eq. (6) would be almost $\pi/2$ and thus dq_{i-j} determined by Eq. (6) would be a small value. In addition, when considering the radiant heat exchange, the amount of time needed to calculate precise result would equate to ten times of that for the calculation without considering the radiant heat exchange. Hence in this study we investigated the effects of the radiant heat exchange on the simulated temperature distribution in the cell only for one calculating condition, and in a parametric study for the effects of the calculating conditions on the cell performance, we neglected the radiant heat exchanges inside the channels to reduce the calculation time.

The radiant losses from the unit surface to the environment were neglected in this model, since the singleunit considered is far from the stack surface and thus the unit surface is regarded to be thermally adiabatic. Accordingly the whole energy balance equation in the steady state was simplified as follows:

$$H_A^{OUT} + H_F^{OUT} = H_A^{IN} + H_F^{IN} \tag{9}$$

2.3. Electrochemical model

The reactions taken into account are (at anode) as follows:

Steam reforming reaction:

$$CH_4 + H_2O \leftrightarrow CO + 3H_2 \tag{10}$$

Shift reaction:

$$H_2O + CO \leftrightarrow H_2 + CO_2 \tag{11}$$

Electrochemical oxidation:

$$H_2 + O^{2-} \rightarrow H_2O + 2e^- \tag{12}$$

$$CO + O^{2-} \rightarrow CO_2 + 2e^- \tag{13}$$

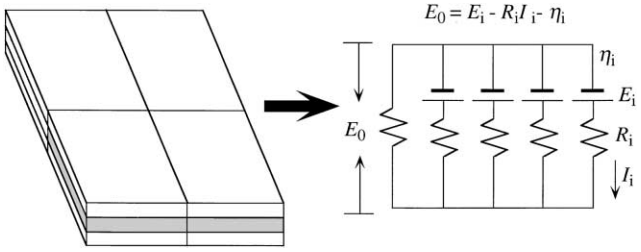

Fig. 4. The discrete anode/electrolyte/cathode unit and the equivalent circuit.

At the cathode,

$$\tfrac{1}{2}O_2 + 2e^- \rightarrow O^{2-} \tag{14}$$

Electrochemical reactions were assumed to be instantaneous at both electrodes and occur at the interfaces between electrodes and electrolyte. It has been reported that the shift reaction is fast enough [11] and in this model we assumed that the shift reaction is in chemical equilibrium at any point in the anode.

For the calculation of the electric current, we considered a discrete anode/electrolyte/cathode unit shown in Fig. 4. The direction of the electric current path in the electrolyte was vertical to the interfaces between the electrolyte and electrodes, and the in-plane path was treated as negligible. The electric current I_i in the ith discrete cell was determined by the operating cell voltage E_0 as follows:

$$E_0 = E_i - R_i I_i - \eta_i \tag{15}$$

where E_i is the Nernst potential, R_i is the Ohmic resistance, and η_i is the overpotential. The calculated Nernst potentials include the concentration overpotential in itself and thus h_i mainly consists of the activation overpotential. In some models for the cell performance, the resistance of the cell has been estimated by considering subdivision of the cell into the cell components (i.e. electrolyte, anode, cathode, and inter-connector) [12,13]. However, in a practical cell-stack, contact resistances among each cell component are usually not negligible and the experimentally measured cell resistance would contain the contact resistances. Accordingly, in the present model, we employed the resistance for a single-cell (anode/electrolyte/cathode), which was estimated from the experimentally measured I–V data for a single-cell. The measured performance of the single-cell modeled in this simulation is shown in Fig. 5. A value of 50 mV was used as the current-independent term of η_i, and the current-dependent term was included in a formula of the Ohmic resistance. Using the empirical formula, the sheet resistance r_i was expressed as follows:

$$r_i = \frac{T}{-34 + 1.25 \times 10^6 \times \exp(-7185/T)} + 0.04 \tag{16}$$

Supposing that no temperature gradients are present in the discrete anode/electrolyte/cathode unit, the Nernst potential is a function of the average temperature T_i in the ith anode/electrolyte/cathode unit and the oxygen partial pressure p_{O_2}

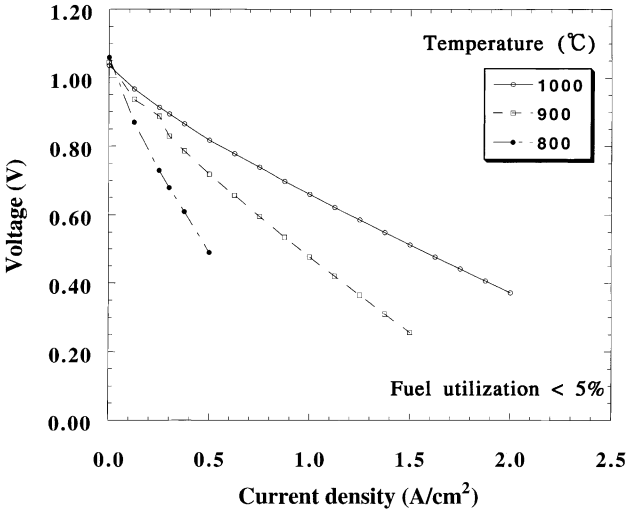

Fig. 5. Performance of a single-cell at 800, 900, and 1000°C.

at both the electrodes. Accordingly the Nernst potential is given as

$$E_i = \frac{FRT}{4F} \ln \frac{p_{O_2(c)}}{p_{O_2(a)}} \tag{17}$$

where R is the gas constant, F the Faraday constant, and $p_{O_2(c)}$ and $p_{O_2(a)}$ are the partial pressure of oxygen at the electrolyte/cathode and electrolyte/anode interfaces, respectively.

For the steam reforming reaction [10] at the anode, some formulae describing the reaction rate have been proposed [14,15]. We measured the reaction rate for the methane reforming reaction using a Ni/YSZ cermet, and in the present model we used the following empirical formula as the reaction rate:

$$r(1) = k_0 \exp\left(\frac{-\Delta E}{RT}\right) p_{CH_4}^{1.3} p_{H_2O}^{-1.2} D_a \tag{18}$$

where ΔE is the activation energy, k_0 a constant, p partial pressure, and D_a the density of the anode. The equilibrium constant for the shift reaction [11] is expressed as

$$K_{shift} = \exp\left(\frac{-\Delta H_0}{RT} - \frac{\Delta\alpha - \Delta S_0}{R} + \frac{\Delta\alpha \ln T}{R} + \frac{\Delta\beta}{2R}T + \frac{\Delta\gamma}{6R}T^2\right) \tag{19}$$

where ΔH_0 is the heat of reaction, ΔS the entropy change, α, β, and γ the coefficients of the temperature-dependent terms in the function for the specific heat.

The reaction rates of the shift reaction [11] are determined for the forward and the backward processes:

$$r(2)_f = k_1 p_{CO} p_{H_2O} \tag{20}$$

$$r(2)_b = k_1 K_{shift} P_{CO_2} P_{H_2} \tag{21}$$

where k_1 is a constant.

The parameters used in Eqs. (18)–(21) are listed in Table 1.

The electric current density J is expressed by Faraday's law:

$$J = 4F\frac{dO_2}{dt} = 2F\frac{df}{dt} \tag{22}$$

where dO_2/dt and df/dt are the molar flux rates of oxygen and fuel at the cathode and the anode, respectively. Matsuzaki and Yasuda have reported that the electrochemical oxidation rate of H_2 is about two times higher than that of CO [16]. As a consequence, in this model, we assumed that H_2 consumption rate was double of CO consumption rate. If the shift reaction is fast enough, the shift reaction will be in the equilibrium state in the anode, and as a result, the assumption for the ratio of the H_2 consumption to the CO consumption will not affect the simulation.

The diffusion of the gaseous species in the porous electrodes was considered by specifying the molecular diffusivity for the each specimen and specifying the momentum source term in a linearized form. The detail of the calculation for the diffusion of the gaseous species in the porous electrodes was reported elsewhere [17].

2.4. Thermal stress calculation

The principal stress in the solid part was calculated from the simulated temperature distribution in the solid part using the finite element program 'ABAQUS' (Hibbit, Karlsson and Sorensen Inc.). In the stress calculation, the discrete 3-D meshes used for the thermo-fluids analysis were employed, and the element type was 3-D solid elements of eight-node linear brick. The calculated temperatures were read into the ABAQUS at the nodes and they were then interpolated to the calculation points within elements. In the stress calculation, it was assumed that no mechanical loads were put on the cell components and the cell components could deform freely, i.e. no constraint condition. The cell operating conditions and parameters used for the simulation are listed in Table 2.

Table 1
Parameters for the chemical reactions

D_a (kg/m^3)	k_0 (mol/kg)	ΔE (J/K mol)	ΔH_0 (J)	ΔS (J)	$\Delta\alpha$ (J)	$\Delta\beta$ (J)	$\Delta\gamma$ (J)	k_1 (mol/m^3 s)
9.3×10^2	1.09×10^{10}	1.91×10^5	-4.179×10^4	-4.337×10^1	-9.306×10^{-1}	2.382×10^{-2}	-1.220×10^{-5}	1.2×10^4

Table 2
The cell operating conditions and parameters used for the simulation

Sample number	Fuel			Air		Channel length (mm)	Thermal conductivity (W/m/K)		Flow pattern	Operating voltage (V)
	Velocity (m/s)	Temperature (K)	Composition[a]	Velocity (m/s)	Temperature (K)		Separator	Electrolyte		
1	0.4	1273	2	3	1123	100	1.8	2.25	counter-flow	0.7
2	0.57	1273	Pre-reformed	3	1123	100	1.8	2.25	counter-flow	0.7
3	0.4	1273	2	3	1123	100	10	2.25	counter-flow	0.7
4	0.4	1273	2	3	1173	100	1.8	2.25	co-flow	0.7
5	1.2	1273	2	9	1123	300	1.8	2.25	counter-flow	0.7
6	0.4	1273	2	3	1123	100	1.8	2.25	counter-flow	0.65

[a] The ratio H_2O/CH_4.

3. Results and discussion

3.1. Thermo-fluid analysis

We first specified the standard cell operating conditions and parameters for the counter-flow case so that the fuel utilization would be around 80% (the flow rate of air was set so that the oxygen utilization would be around 30%). With the selected parameters for the operating conditions, the concentrations of the gaseous species, the Nernst potential, the distribution of the current density, the average current density, the overall fuel utilization, and the temperature distribution were calculated. Fig. 6(a)–(d) show the calculated concentration profile for CH_4, H_2, CO, and H_2O at the anode, respectively. Here it should be noted that in this calculation we neglected the radiant heat exchange inside the channels. It can be seen that most of the supplied CH_4 is reformed within the first 10 mm from the fuel inlet, suggesting that the steam reforming reaction is much faster than the velocity of the fuel flow. Consequently, H_2 and CO concentrations rapidly increase within this area, and then gradually decrease as a result of consumption by the electrochemical oxidation while flowing towards the fuel outlet. In the area underneath the inter-connector rib, the gaseous species are transported only by diffusion in the porous electrodes. This leads to the lower H_2 and CO and higher H_2O concentrations than in the channel area. Although in the present analyses we did not study the effect of the rib width on the cell performance, the increase of the overall potential drop with the increase of the rib width has been reported [18]. At the fuel outlet, 80% of the supplied fuel has been consumed.

At just a short distance from the fuel inlet, the cell temperature drops rapidly because of the endothermic steam

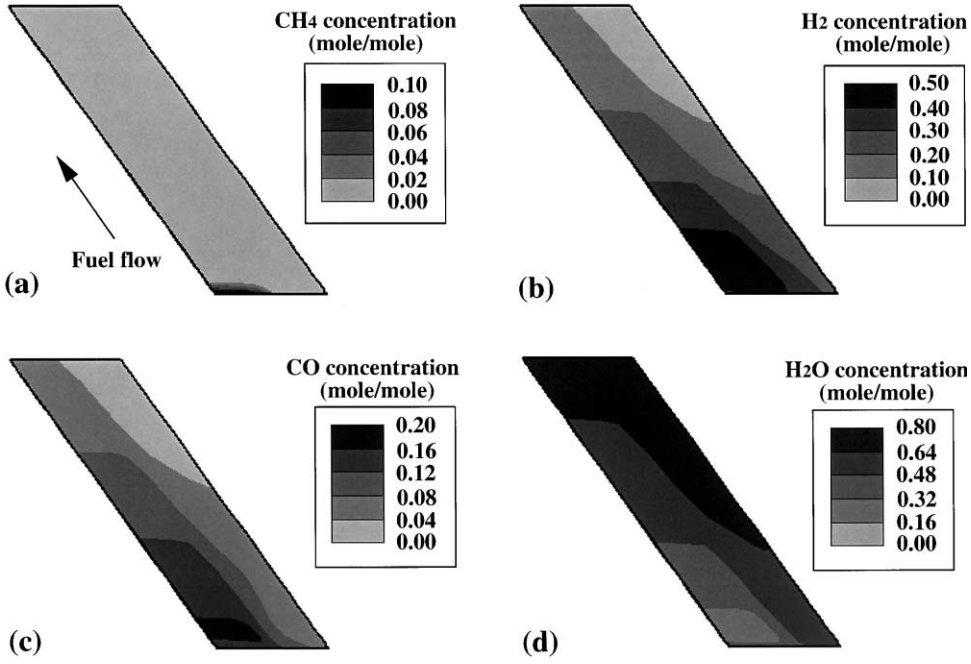

Fig. 6. The calculated profiles of CH_4, H_2, CO, and H_2O concentrations in the anode for the standard case (no. 1).

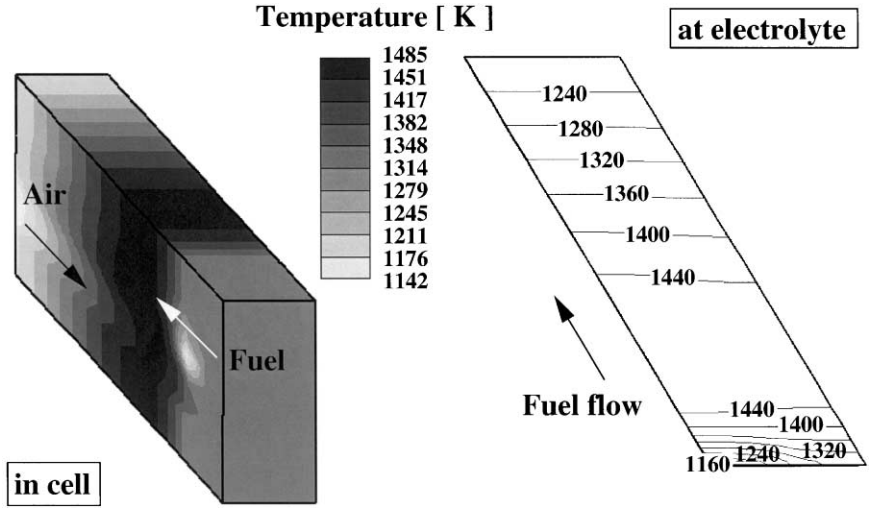

Fig. 7. The simulated temperature profiles in the cell and at the electrolyte for the standard case (no. 1) without a consideration of the radiant heat exchange.

reforming reaction as shown in Fig. 7. In the middle area where the steam reforming reaction is complete, the cell temperature rises because of the exothermic electrochemical reaction. At the downstream of the fuel, the cell temperature decreases along the fuel stream, since the heat generation is small and in addition, the hot fuel is cooled by the incoming air. Here we comment on the effect of the radiant heat exchange inside the channels on the simulated temperature distribution in the cell. Fig. 8 shows the temperature distribution at the electrolyte calculated with considering the radiant heat exchange inside the channels. As comparing Fig. 8 with Fig. 7, we can see two characteristic features. One is that when the radiant heat exchange is taken into consideration, the temperature distribution in the cell becomes flat. This comes from that the radiant heat exchange occurs when the temperatures in the channels differ between high and low temperature volumes. As compared the maximum temperature in the cell for $\varepsilon = 0$ and $\varepsilon = 0.8$, the difference in the temperature is 30 K. The value of 30 K equates about 10% of the difference in the temperature along the fuel flow at the electrolyte. A further difference is that when the radiant heat exchange is considered, the area where the temperature is the maximum moves to the fuel downstream. When the radiant heat exchange is not considered, the areas with the maximum and the minimum temperature are very close as we can see in Fig. 7. When the radiant heat exchange is considered, a radiant heat loss at the hottest area is larger because the temperature is higher and the radiation angle ϕ is close to zero as shown in Fig. 9. With increasing the distance from the fuel inlet where the temperature is the minimum to the area with the maximum temperature, the value of the radiant

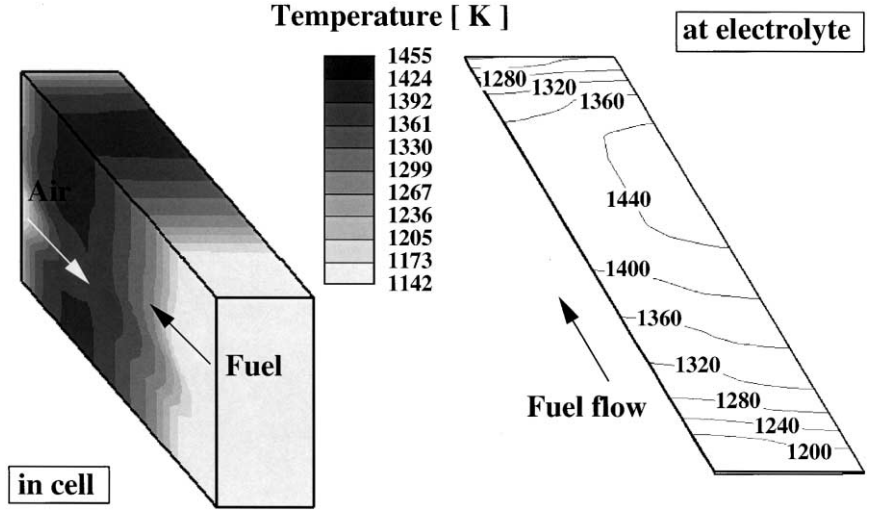

Fig. 8. The simulated temperature profiles in the cell and at the electrolyte for the standard case (no. 1) with a consideration of the radiant heat exchange of $\varepsilon = 0.8$.

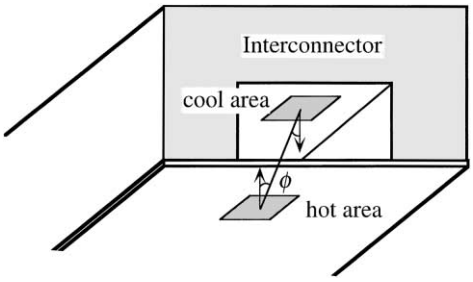

Fig. 9. The illustration of the radiant heat exchange between areas with high and low temperatures near the fuel inlet.

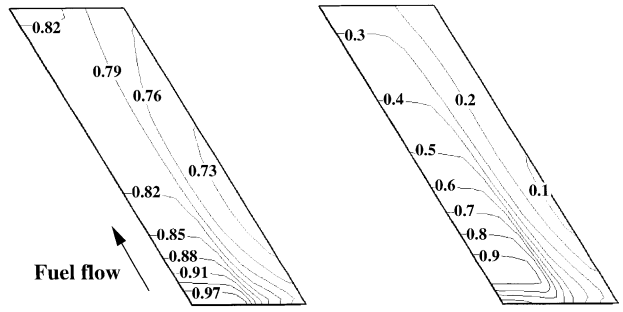

Fig. 10. The calculated Nernst potential profile (a) and current density profile; (b) at the electrolyte/anode interface for the standard case (no. 1).

heat exchange becomes small. Thus the area with the maximum temperature may shit to the downstream of the fuel flow when the radiant heat exchange is considered.

Fig. 10(a) and (b) indicate the Nernst potential and current density profile at the electrolyte/anode interface, respectively. The Nernst potential decreases along the fuel stream, reflecting the decrease of the H_2 and CO concentrations. Reflecting the lack of H_2 and CO, the Nernst potential is lower in the area underneath the inter-connector rib than in the channel. At the fuel inlet, instead of the high potential, the current density is not so high because the cell temperature is low and thus the cell resistance is high. Along the fuel flow, the current density once increases and reaches a maximum value of about 0.9 A/cm^2. At the fuel downstream, both the cell temperature and Nernst potential is lower, accordingly the current density become a lower value. Although the maximum current density is as high as 0.9 A/cm^2, the minimum current density value is as low as 0.073 A/cm^2 in the area underneath the inter-connector rib and thus the average current density comes down to 0.39 A/cm^2.

Next we focus on the effects of the gas flow pattern. When the air inlet temperature in the co-flow pattern is the same as in the standard case (counter-flow pattern), the drop of the electrolyte temperature due to the endothermic steam reforming is larger, resulting in an increase of the sheet resistance. Accordingly, the fuel utilization becomes smaller than in the standard case. In order to increase the fuel utilization to that in the standard case, the air inlet temperature has been modified to be 1173 K. All other operating conditions are the same as in the standard case. Fig. 11 exhibits the temperature profile in the cell and at the electrolyte for the co-flow case. In contrast to the standard counter-flow case, the electrolyte temperature increases monotonically from the fuel inlet to the fuel outlet. As a result, the potential keeps a high value from the fuel inlet to the middle area of the fuel flow, and decreases rapidly near the fuel outlet as shown in Fig. 12(a). Although the current density profile shows a maximum value in the middle area as well as in the standard case, the difference between the maximum and the minimum current densities, 0.46 A/cm^2, is smaller than 0.88 A/cm^2 in the standard case as can be seen in Fig. 12(b).

All the simulated results for the selected cases in Table 2 are summarized in Table 3. To validate the numerical simulation for the cell performance, a benchmark test on

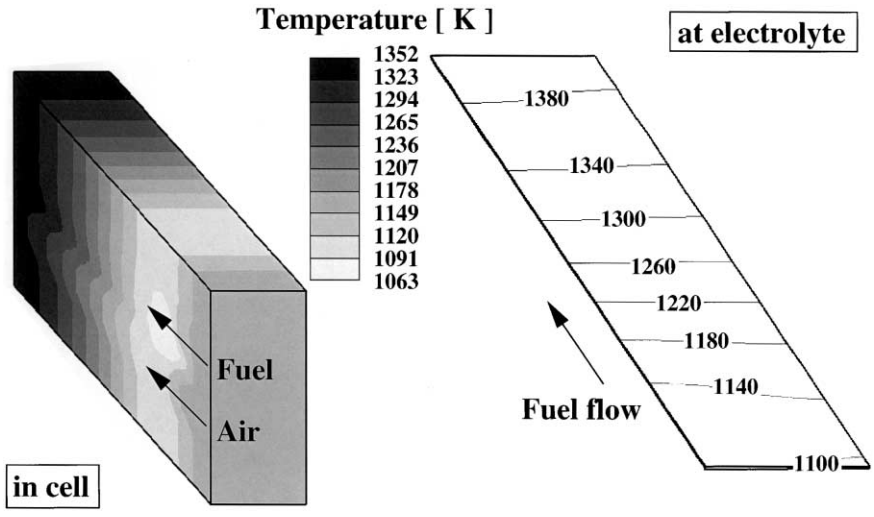

Fig. 11. The simulated temperature profile in the cell and at the electrolyte for the co-flow case (no. 4).

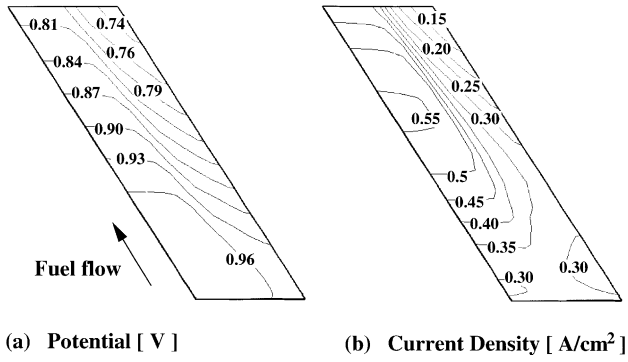

Fig. 12. The calculated Nernst potential profile (a) and current density profile; (b) at the electrolyte/anode interface for the co-flow case (no. 4).

the numerical model for the cell performance has been carried out by International Energy Agency (IEA) participants [12]. Since the calculating conditions (e.g. the temperatures of the introduced fuel and air, the fuel composition, the single-cell properties, the cell operating voltage and thus the fuel utilization) in the present simulation are different from those in the IEA benchmark test, the present results cannot be compared quantitatively with the results obtained by IEA. However, the present results such as the concentration profile for the gaseous species, and the reduction of the temperature difference in the cell by employing the co-flow pattern are qualitatively agree with the previously reported results [12].

3.2. Stress calculation

We calculated the thermally induced stresses in the electrolyte and the inter-connector for the six cases in Table 2. The distributions of the principal stresses in the electrolyte and the inter-connector were calculated from the simulated temperature distributions. The results for the standard case are shown as an example in Fig. 13. We can see a stress concentration near the fuel inlet coming from the steep temperature drop caused by the endothermic steam reforming reaction. The maximum principal stress in the inter-connector is about 2 MPa, which is low enough to avoid damage in the inter-connector. On the other hand, the principal stress in the electrolyte is almost 70 MPa.

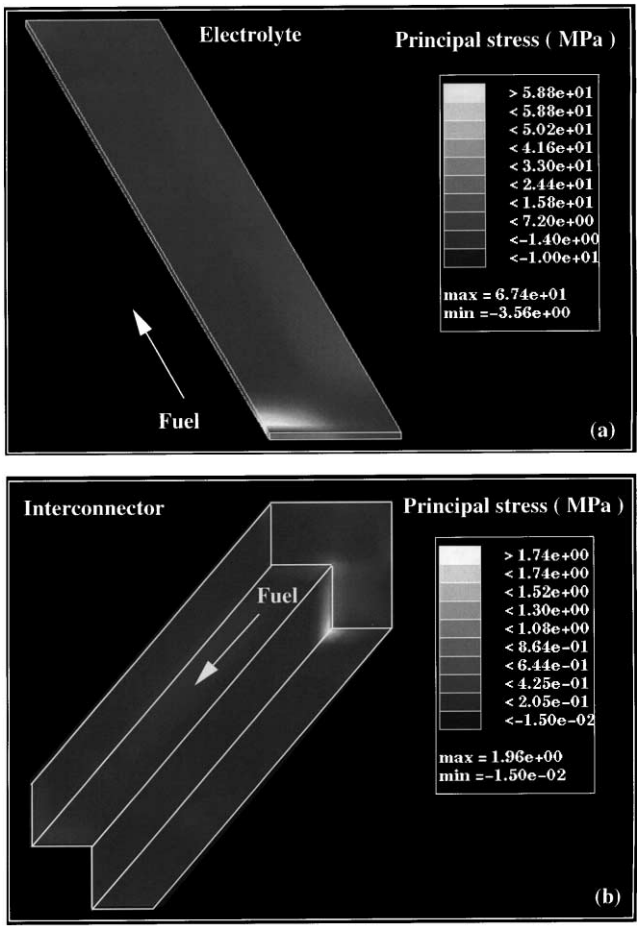

Fig. 13. The tensile stress profiles in the electrolyte (a) and the inter-connector; (b) for the standard case (no. 1).

When 8YSZ is used as the electrolyte, the internal stress would cause cracks or destruction of the electrolytes. Because in our measurement for the tensile strength on the tape-cast 8YSZ, the compensated tensile strength of the electrolyte sheets at room temperature were estimated to be about 80 MPa [19], and it has been reported that the mechanical strength of 8YSZ becomes low at high temperatures [20,21]. All the calculated maximum tensile stresses in the electrolyte and the inter-connector for the six cases listed in Table 2 are summarized also in Table 3. For all the cases,

Table 3
Comparison of the simulated results

Sample number	Fuel utilization (%)	Average current density (A/cm^2)	Cell temperature (K)			Maximum tensile stress (MPa)	
			At fuel outlet	At air outlet	Maximum	In separator	In electrolyte
1	79	0.398	1213	1326	1488	1.96	67
2	77	0.308	1200	1511	1536	0.57	7.7
3	82	0.41	1291	1320	1398	0.45	79
4	77	0.386	1344	1338	1352	0.79	26
5	77	0.386	1162	1331	1571	2.64	95
6	92	0.463	1232	1443	1617	2.41	77

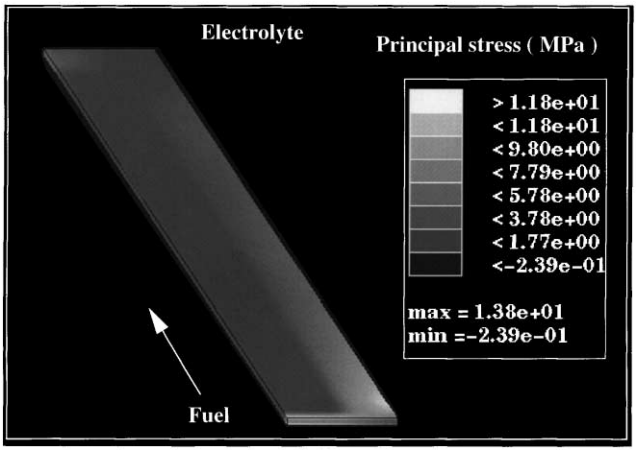

Fig. 14. The tensile stress profile in the electrolyte for the external-reforming case (no. 2).

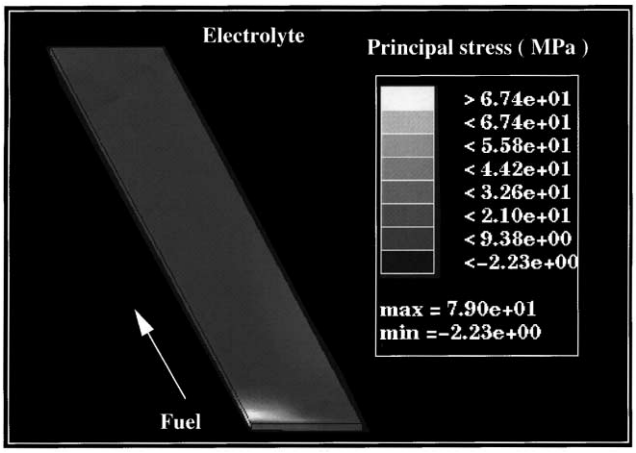

Fig. 16. The tensile stress profile in the electrolyte for the case of using an inter-connector with a high thermal conductivity (no. 3).

the maximum tensile stresses in the electrolyte are several tens MPa while those in the inter-connector are less than several MPa.

The stress concentration would occur near the minimum temperature point, and thus the magnitude of the maximum tensile stress can be related to the magnitude of the steep temperature drop caused by the prevailing steam reforming reaction. For the external reforming case, the maximum tensile stress is one order of magnitude smaller than those for the internal methane reforming cases because there is no steep temperature drops coming from the largely endothermic reaction. In addition, the stress concentration occurs at the different region from that for the internal reforming case as shown in Fig. 14. For the co-flow case, one can see in Fig. 15 that the maximum tensile stress in the electrolyte is notably reduced as compared with the counter-flow case. This comes from the fact that the steam reforming reaction is less prevailing than in the counter-flow case, and the electrolyte temperature gradually increases along the fuel flow as shown in Fig. 11. In case of the inter-connector with a high thermal conductivity, despite that the calculated temperature difference in the cell is smaller, the maximum tensile stress is higher than that for the standard case as shown in Fig. 16. This is attributed to that near the fuel inlet the temperature gradient along the direction perpendicular to the gas flow is steeper. The steeper temperature gradient is due to that the highly thermally conducting inter-connector carries the heat from the high temperature region to the minimum temperature region. Thus these results indicate that the steam reforming reaction is the substantial origin of the thermal stress, and reducing the induced temperature drop near the fuel inlet is an advantageous way to avoid the failure of the electrolyte sheet. If a mechanical load exists or the cell components constrain each other, the maximum stress will increase more. It is, however, possible to reduce the tensile stress in the electrolyte by employing the co-flow pattern.

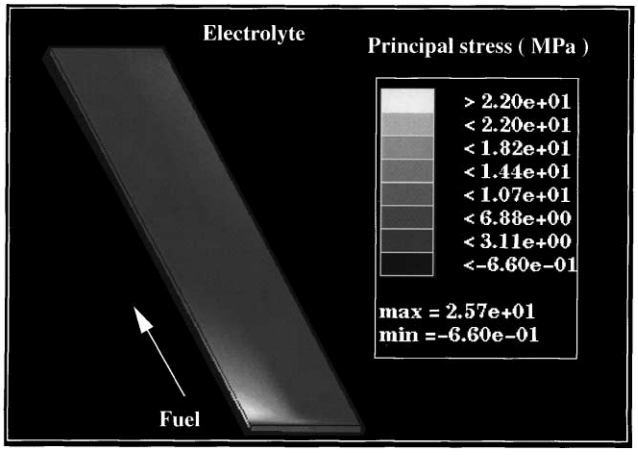

Fig. 15. The tensile stress profile in the electrolyte for the co-flow case (no. 4).

4. Conclusions

The fluid flow phenomena, including heat transfer, mass transfer, and chemical reactions in the planar SOFC were simulated for the simplified single-unit model with the bipolar channels for co-flow or counter-flow pattern. The steam-reforming reaction, the water-shift reaction, and the diffusion of gases in the porous electrode were modeled. The effects of the cell size, the operating voltage, and the thermal conductivity of the cell components on the calculated results were investigated. Using the finite element method, the stress distributions in the electrolytes and the inter-connectors were calculated from the simulated temperature profiles. It was found that the internal reforming would induce a steep drop of fuel temperature near the inlet, resulting in large tensile stresses in the electrolytes. The co-flow pattern is advantageous to mitigate the steep temperature gradient, and hence to reduce the internal stresses.

Acknowledgements

A part of this work was performed as R&D program of New Energy and Industrial Technology Development Organization (NEDO) under the New Sunshine Project of Agency of Industrial Science and Technology, MITI. We would like to thank NEDO and MITI for their advice and financial support.

References

[1] U.G. Bossel, Solid oxide fuel cells III, in: S.C. Signal, H. Iwahara (Eds.), The Electrochemical Society Proceedings Series, Pennington, NJ, USA, 1993, PV 93-4, p. 833.
[2] A. Solheim, Solid oxide fuel cells III, in: S.C. Signal, H. Iwahara (Eds.), The Electrochemical Society Proceedings Series, Pennington, NJ, USA, 1993, PV 93-4, p. 841.
[3] T. Sira, M. Ostenstand, Solid oxide fuel cells III, in: S.C. Signal, H. Iwahara (Eds.), The Electrochemical Society Proceedings Series, Pennington, NJ, USA, 1993, PV 93-4, p. 851.
[4] H. Karoliussen, K. Nisancioglu, Solid oxide fuel cells III, in: S.C. Signal, H. Iwahara (Eds.), The Electrochemical Society Proceedings Series, Pennington, NJ, USA, 1993, PV 93-4, p. 868.
[5] A. Malandrino, M. Chindemi, Solid oxide fuel cells III, in: S.C. Signal, H. Iwahara (Eds.), The Electrochemical Society Proceedings Series, Pennington, NJ, USA, 1993, PV 93-4, p. 885.
[6] M. Bernier, J. Ferguson, R. Herbin, in: P. Stevens (Ed.), European Solid Oxide Fuel Cell Forum III, Nantes, France, 1998, p. 471.
[7] J. Domergue, A. Rufer, N. Buchheit, in: P. Stevens (Ed.), European Solid Oxide Fuel Cell Forum III, Nantes, France, 1998, p. 461.
[8] A. Comte, P. Mathevon, P. Stevens, in: P. Stevens (Ed.), European Solid Oxide Fuel Cell Forum III, Nantes, France, 1998, p. 483.
[9] P.V. Hendriksen, Solid oxide fuel cells V, in: U. Stimming, S.C. Singhal, H. Tagawa, W. Lehnert (Eds.), The Electrochemical Society Proceedings Series, Pennington, NJ, USA, 1997, PV 97-40, p. 1319.
[10] R.P. Travis, E.P. Busso, Yu.V. Tkach, in: S.C. Singhal, M. Dokiya (Ed.), Solid Oxide Fuel Cells VI, The Electrochemical Society Proceedings Series, Pennington, NJ, 1999, PV 99-19, p. 1037,
[11] D. Stolten, D. Froning, L.G. J de Haart, in: A.J. McEvoy (Ed.), European Solid Oxide Fuel Cell Forum IV, Lucerne, Switzerland, 2000, p. 347.
[12] R. Herbin, J.M. Fiard, J.R. Ferguson, in: U. Bossel (Ed.), 1st European Solid Oxide Fuel Cell Forum, Lucerne, Switzerland, 1994, p. 317.
[13] A. Selimovic, in: A.J. McEvoy (Ed.), European Solid Oxide Fuel Cell Forum IV, Lucerne, Switzerland, 2000, p. 375.
[14] E. Achenbach, J. Power Sources 52 (1994) 282.
[15] A.L. Lee, R.F. Zebransky, W.J. Huber, Ind. Eng. Chem. Res. 29 (1990) 766.
[16] Y. Yasuda, I. Matsuzaki, J. Electrochem. Soc. 147 (2000) 1630.
[17] H. Yakabe, M. Hishinuma, M. Uratani, Y. Matsuzaki, I. Yasuda, J. Power Sources 86 (2000) 423.
[18] M. Bernier, R. Herbin, E. Gehain, in: B. Thorstensen, (Ed.), European Solid Oxide Fuel Cell Forum II, Oslo, Norway, 1996, p. 203.
[19] T. Ogiwara, H. Yakabe, M. Hishinuma, I. Yasuda, in: A.J. McEvoy (Ed.), European Solid Oxide Fuel Cell Forum IV, Lucerne, Switzerland, 2000, p. 193.
[20] H. Greiner, E. Keim, W. Kleinlein, E. Weis, in: Solid Oxide Fuell Cells II, F. Grosz, P. Zegers, S.C. Signal, O. Yamamoto, (Eds.), Commission of the European Communities, Athens, Greece, 1991, p. 705.
[21] F.L. Lowrie, R.D. Rawlings, J. Eur. Ceramic Soc. 20 (2000) 751.